

The HSE hybrid functional within the FLAPW method and its application to GdN

Martin Schlipf,* Markus Betzinger, Christoph Friedrich, Marjana Ležaić, and Stefan Blügel
*Peter Grünberg Institut and Institute for Advanced Simulation,
 Forschungszentrum Jülich and JARA, 52425 Jülich, Germany*

We present an implementation of the Heyd-Scuseria-Ernzerhof (HSE) hybrid functional within the full-potential linearized augmented-plane-wave (FLAPW) method. Pivotal to the HSE functional is the screened electron-electron interaction, which we separate into the bare Coulomb interaction and the remainder, a slowly varying function in real space. Both terms give rise to exchange potentials, which sum up to the screened nonlocal exchange potential of HSE. We evaluate the former with the help of an auxiliary basis, defined in such a way that the bare Coulomb matrix becomes sparse. The latter is computed in reciprocal space, exploiting its fast convergence behavior in reciprocal space. This approach is general and can be applied to a whole class of screened hybrid functionals. We obtain excellent agreement of band gaps and lattice constants for prototypical semiconductors and insulators with electronic-structure calculations using plane-wave or Gaussian basis sets. We apply the HSE hybrid functional to examine the ground-state properties of rocksalt GdN, which have been controversially discussed in literature. Our results indicate that there is a half-metal to insulator transition occurring between the theoretically optimized lattice constant at 0 K and the experimental lattice constant at room temperature. Overall, we attain good agreement with experimental data for band transitions, magnetic moments, and the Curie temperature.

PACS numbers: 71.15.-m, 71.15.Ap, 71.15.Mb, 31.15.E-

I. INTRODUCTION

Density functional theory (DFT)^{1,2} is a powerful tool for calculating the electronic ground-state properties of molecules and solids. The predictive power of numerical DFT calculations relies on the availability of accurate approximations for the exchange-correlation (xc) energy E_{xc} , which incorporates all complicated many-body effects. In many systems, this quantity is described adequately by the local-density approximation (LDA).³⁻⁵ However, in more complex systems, physical properties such as the geometric structure, magnetic properties, and the band gap are not well reproduced. One can go beyond the LDA by taking into account the local density gradient, which yields the generalized gradient approximation (GGA),^{6,7} upon which many functionals are based. However, despite their success, the GGA functionals still often fail in describing systems with localized states, which is attributed to an incomplete cancellation of the self-interaction error in these semi-local functionals.^{8,9}

This deficiency is particularly critical in systems whose electronic properties are largely governed by the correlated motion of electrons in localized states. The rare-earth chalcogenides are among this class of materials, having incompletely filled f -electron shells. They are insulating, semiconducting, or metallic depending on details of the valency of the rare-earth element. Gadolinium nitride (GdN) is widely studied owing to the ferromagnetic order, large magnetic moment of $6.88 \mu_B$ per Gd atom¹⁰ and its large magnetoresistive effect,¹¹ which makes the material interesting for technological applications. The mechanism of the ferromagnetic order is still under debate. Various types are being discussed, such as carrier mediated^{12,13} and superexchange mechanisms.¹⁴ Another point of debate are the electronic properties.

It was experimentally demonstrated to be a low carrier semimetal in single crystals¹⁵ and insulating in thin films.¹⁶ There are also several recent reports of thin films of GdN having a degenerately doped semiconducting¹⁷⁻¹⁹ or a metallic ground state¹⁹ based on the resistivity data measured at low temperatures. Theoretically it is predicted to have a semiconducting^{20,21} or a half-metallic character^{14,22,23} based on *ab initio* calculations.

Materials with strongly localized states, such as the f states in GdN, are often treated within the LSDA+ U method,²⁴ where the electron correlation in these states is described with an additional on-site term, that involves the Hubbard parameter U . The disadvantage of this method is that the value of U is not known a priori. Although methods to estimate the U value from first-principles calculations have been developed,²⁵⁻²⁷ it is usually chosen to reproduce experimental observations. However, a specific U value that provides a good description of one quantity is often not suitable to describe another quantity.²⁸

During the last decade, hybrid functionals that combine a fraction of nonlocal Hartree-Fock (HF) exchange with local xc functionals have been shown to be a viable improvement over LDA and GGA offering a parameter-free description specifically suited for band gap materials.^{29,30} The explicit consideration of nonlocal HF exchange leads to a partial cancellation of the self-interaction error, but also makes numerical calculations considerably more demanding than conventional LDA and GGA calculations. Various hybrid functionals have been developed. In empirical hybrid functionals, such as the B3LYP functional,³¹ the fraction of HF exchange is determined by fitting to an experimental data set. In the PBE0 functional³² the mixing parameter for the HF exchange is inferred from expanding the inte-

grand of the adiabatic-connection formula of the exact xc functional.

In periodic systems, the Coulomb interaction between the electrons is effectively screened by polarization effects in the electron system. The effective interaction is particularly short-ranged in systems with small or vanishing band gaps. Therefore, Heyd *et al.*³³ introduced a range-separated hybrid functional, which has the added benefit to reduce the computational cost within a basis of localized Gaussian functions. Starting from the PBE0 functional, they partitioned the Fock exchange term into a short- and a long-range part, where the former is described by a correspondingly screened Fock term and the latter is treated by a local approximation, derived from the PBE functional.⁷ Heyd *et al.* showed that this hybrid functional leads to a reduced computational demand for localized basis sets compared with the PBE0 functional. Furthermore, it even yields results which are often in better agreement with experiment.³⁰

The Heyd-Scuseria-Ernzerhof (HSE) hybrid functional has been implemented within Gaussian³³ and plane-wave^{34,35} basis sets. In this work, we present an implementation within the full-potential linearized augmented-plane-wave (FLAPW) approach as implemented in the **Fleur** code,³⁶ which provides a highly accurate all-electron basis^{37–39} for a large variety of materials, including open systems with low symmetry, *d*- and *f*-electron systems, as well as oxides and nitrides. An implementation of the PBE0 functional limited to certain localized states and on-site interactions was given by Tran *et al.*⁴⁰ Betzinger *et al.*⁴¹ described an efficient way to calculate the full nonlocal exchange potential for the PBE0 functional without these restrictions. Very recently, Tran and Blaha⁴² reported an implementation of hybrid functionals whose nonlocal exchange integrals are evaluated using the pseudocharge method of Weinert.⁴³ However, this approach mathematically restricts the electron-electron interaction to potentials that are solutions of Laplace-type equations, whose radial solutions can be expressed as analytically or numerically known regular and irregular solutions and spherical harmonics, such as the bare Coulomb and the screened Yukawa potential. The error function used in the HSE functional does not have this property. In our implementation, there is no such restriction. Our approach is very general. In fact, any kind of interaction potential can be implemented for the nonlocal exchange potential by changing only a single line of code. The only requirement is that it differs from the bare Coulomb potential by a function that possesses a fast Fourier expansion, a condition that is fulfilled by all physical screened potentials, including the error function used in the HSE functional.

Our numerical approach extends the implementation of Ref. 41, which is based on an auxiliary basis that is designed to represent products of wave functions. This so-called mixed product basis (MPB) is constructed directly from products of LAPW basis functions and retains the full accuracy of the all-electron description. Several tech-

niques were introduced to accelerate the evaluation of the computationally expensive nonlocal exchange term. Spatial and time-reversal symmetries are exploited to restrict the Brillouin-zone (BZ) summations to irreducible sets of **k**-points. The nonlocal potential is calculated in the basis of single-particle eigenstates, which allows to truncate the matrix at a certain number of bands. The divergence of the Coulomb potential in the BZ center is treated analytically instead of using dense **k**-point sets around **k** = **0**. A nested density convergence scheme greatly reduces the number of iterations in the self-consistent field cycle. Finally, by a suitable transformation of the MPB the Coulomb matrix becomes sparse, which speeds up the matrix-vector operations considerably.

This transformation relies on the analytic properties of the bare Coulomb potential. Any other potential, in particular the screened Coulomb interaction, will not lead to a sparse matrix representation, though. Furthermore, in contrast to Gaussian or plane-wave basis sets, a direct evaluation of the screened Coulomb matrix, in the same way as for the bare Coulomb matrix,⁴⁴ is cumbersome in the MPB. Therefore, we incorporate the screening, after calculating the bare nonlocal exchange potential, in a separate step, which produces hardly any overhead. In this way, the simple analytic properties of the bare Coulomb potential as well as the sparsity of the Coulomb matrix are retained and can be taken advantage of.

We validate our implementation by comparing results for prototypical semiconductors and insulators with results from the literature. Then, we calculate the ground-state properties and the band structure of GdN. The band gap of GdN is controversially discussed in literature. Results from LSDA+*U* calculations are inconclusive. While the linearized muffin-tin orbital (LMTO) approach yields a narrow-gap semiconductor as ground state,^{12,20,45,46} GdN exhibits a transition from a half-metallic to a semiconducting ground state under strain within the FLAPW method.¹⁴ Two different solutions close in energy were obtained in an investigation using the hybrid functional B3LYP.²³ Both solutions were half-metallic, one in the majority spin channel, the other one in the minority spin channel. Our results show a transition from a half-metallic ground state, which is similar to the energetically slightly less favorable solution of Ref. 23, to a semiconductor under strain as in the LSDA+*U* calculation of Ref. 14. In their work, a large change of the lattice constant of more than 10% was necessary to observe this transition. However, our calculations indicate that already small volume changes ($\approx 0.5\%$) are sufficient to observe this transition.

The paper is organized as follows. In Sec. II, we give a brief introduction to the theory of hybrid functionals. In Sec. III, we introduce the FLAPW method and describe our implementation of the HSE functional. In Sec. IV, we first compare results for prototypical semiconductors and insulators with values from the literature. Then, we present our findings for GdN in Sec. V. In Sec. VI, we draw our conclusions.

II. THEORY

The construction of hybrid functionals as mixtures of local functionals with a nonlocal exchange term is motivated by the adiabatic-connection formula,^{4,47,48} in which the scaling of the electron-electron interaction establishes a connection between the noninteracting Kohn-Sham system with the fully interacting one. In the weakly interacting limit, the formula becomes identical to the HF exchange term which prompted Becke^{31,49} to introduce a certain fraction a of HF exchange into the xc functional

$$E_{xc}^{\text{HYB}} = E_{xc}^{\text{L}} + a (E_{\text{x}}^{\text{HF}} - E_{\text{x}}^{\text{L}}), \quad (1)$$

where E_{xc}^{L} denotes the local xc functional and E_{x}^{L} its exchange part. E_{x}^{HF} is the HF exchange energy

$$E_{\text{x}}^{\text{HF}} = -\frac{1}{2} \sum_{\sigma} \sum_{\mathbf{k}, \mathbf{q}} \sum_{n, n'}^{\text{BZ occ.}} \iint d^3r d^3r' \varphi_{n\mathbf{k}}^{\sigma*}(\mathbf{r}) \varphi_{n'\mathbf{q}}^{\sigma}(\mathbf{r}) v(|\mathbf{r} - \mathbf{r}'|) \varphi_{n'\mathbf{q}}^{\sigma*}(\mathbf{r}') \varphi_{n\mathbf{k}}^{\sigma}(\mathbf{r}'), \quad (2)$$

evaluated with the Kohn-Sham wave functions $\varphi_{n\mathbf{k}}^{\sigma}(\mathbf{r})$ of spin σ , wave vector \mathbf{k} , and band index n . The sums over \mathbf{k} and \mathbf{q} run over the full Brillouin zone (BZ), n and n' sum over all occupied states, and $v(r) = 1/r$ is the bare Coulomb potential. Here and in the following, atomic units are used unless stated otherwise. As the wave functions $\varphi_{n\mathbf{k}}^{\sigma}(\mathbf{r})$ are functionals of the effective potential, which in turn is a functional of the density, E_{x}^{HF} is a true functional of the density, too.

Perdew *et al.*³² deduced a mixing parameter $a = 0.25$ by assuming a certain shape for the adiabatic-connection integrand. They proposed to use the Perdew-Burke-Ernzerhof (PBE) functional⁷ for the local part. The resulting functional

$$E_{xc}^{\text{PBE0}} = E_{xc}^{\text{PBE}} + a (E_{\text{x}}^{\text{HF}} - E_{\text{x}}^{\text{PBE}}) \quad (3)$$

is nowadays referred to as PBE0.

As the long-range part of the nonlocal HF term is cumbersome to calculate, Heyd *et al.*^{33,50} suggested to replace it again by a simple local functional. Later, it was demonstrated³⁰ that this leads to an improved description of the band gaps of semiconductors. Heyd *et al.*³³ used the error function $\text{erf}(x)$ and its complement $\text{erfc}(x) = 1 - \text{erf}(x)$ to decompose the Coulomb interaction into a long-range (LR) and a short-range (SR) part

$$v(r) = \frac{\text{erf}(\omega r)}{r} + \frac{\text{erfc}(\omega r)}{r} = v^{\text{LR}}(r) + v^{\text{SR}}(r), \quad (4)$$

where ω is an adjustable screening parameter. The HSE hybrid functional is thus given by

$$E_{xc}^{\text{HSE}}(\omega) = E_{xc}^{\text{PBE}} + a [E_{\text{x}}^{\text{HF,SR}}(\omega) - E_{\text{x}}^{\text{PBE,SR}}(\omega)], \quad (5)$$

where $E_{\text{x}}^{\text{HF,SR}}(\omega)$ corresponds to Eq. (2) with the bare Coulomb potential $v(r)$ replaced by $v^{\text{SR}}(r)$. $E_{\text{x}}^{\text{PBE,SR}}(\omega)$

is the local functional for the SR exchange according to the decomposition given in Eq. (4). Its numerical treatment is discussed in Refs. 33 and 51. Based on numerical fits to benchmark data sets of molecules, Heyd *et al.*³³ found an optimized value for the screening parameter $\omega = 0.15$. In this work, we employ the value of $\omega = 0.11$, which was optimized for solids.⁵²

Hybrid functionals are usually applied within the generalized Kohn-Sham formalism,⁵³ which is based on a fictitious system of noninteracting electrons. These particles move subject to a nonlocal potential that is defined in such a way that the electron density $n(\mathbf{r})$ equals that of the real system. The nonlocal potential contains a local part that consists of the external potential created by the nuclear charges, the Hartree potential, i.e., the electrostatic potential produced by the total electron charge density, and a local contribution that derives from functional differentiation of the local parts of Eq. (3) and (5) for the PBE0 and HSE functionals, respectively. The implementation of this local part of the xc potential requires only minor modifications of the DFT code, and we will focus on the nonlocal part in the following, which derives from the nonlocal exchange energy functional E_{x}^{HF} . Leaving out the scaling factor a , its matrix representation in the basis of Kohn-Sham eigenstates is given by

$$V_{x,nn'}^{\sigma,\text{NL}}(\mathbf{k}) = - \sum_{\mathbf{q}} \sum_m^{\text{BZ occ.}} \iint d^3r d^3r' \varphi_{n\mathbf{k}}^{\sigma*}(\mathbf{r}) \varphi_{m\mathbf{q}}^{\sigma}(\mathbf{r}) v(|\mathbf{r} - \mathbf{r}'|) \varphi_{m\mathbf{q}}^{\sigma*}(\mathbf{r}') \varphi_{n'\mathbf{k}}^{\sigma}(\mathbf{r}'). \quad (6)$$

For the HSE functional, the bare interaction $v(r)$ would have to be replaced by the screened interaction $v^{\text{SR}}(r)$. Yet in practice, we first evaluate the nonlocal potential in the form of Eq. (6) and correct for the screening afterwards by subtracting $v^{\text{LR}}(r)$, as will be explained in the next section.

III. IMPLEMENTATION

A. Basis sets

Our implementation of the HSE functional is based on the all-electron FLAPW method,³⁷⁻³⁹ in which space is partitioned into non-overlapping atom-centered muffin-tin (MT) spheres and the remaining interstitial region (IR). The core states, which are confined to the spheres, are obtained from solving the fully relativistic Dirac equation. For the valence and conduction states we use a set of basis functions that are defined differently in the two regions of space: plane waves $e^{i(\mathbf{k}+\mathbf{G})\cdot\mathbf{r}}$ with $|\mathbf{k}+\mathbf{G}| \leq G_{\text{max}}$ in the IR and linear combinations of $u_{lp}^{a\sigma}(r)Y_{lm}(\hat{\mathbf{r}})$ in the MT spheres, where r is measured from the sphere center, $u_{lp}^{a\sigma}(r)$ are numerical functions defined on a radial grid, $Y_{lm}(\hat{\mathbf{r}})$ are spherical harmonics with angular-momentum quantum numbers $0 \leq l \leq l_{\text{max}}$ and $|m| \leq l$, a labels the atom in the unit cell, and p

is an index for different radial functions. G_{\max} and l_{\max} are cutoff parameters. The linear combinations are such that the basis functions and their radial derivatives are continuous at the MT sphere boundaries.

As in Ref. 41, we evaluate the nonlocal potential, Eq. (6), with the help of an auxiliary basis $\{M_{\mathbf{q}J}(\mathbf{r})\}$ and its bi-orthogonal set $\{\tilde{M}_{\mathbf{q}J}(\mathbf{r})\}$, where \mathbf{q} is a Bloch vector and J is used to index these basis functions. By placing the completeness relation

$$1 = \sum_{\mathbf{q}J} |M_{\mathbf{q}J}\rangle \langle \tilde{M}_{\mathbf{q}J}| = \sum_{\mathbf{q}J} |\tilde{M}_{\mathbf{q}J}\rangle \langle M_{\mathbf{q}J}| \quad (7)$$

at both sides of $v(r)$, the six-dimensional integral becomes a sum over vector-matrix-vector products in the space of the MPB

$$V_{x,nn'}^{\sigma,\text{NL}}(\mathbf{k}) = - \sum_m^{\text{occ.}} \sum_{\mathbf{q}}^{\text{BZ}} \sum_{IJ} \langle \varphi_{n\mathbf{k}}^{\sigma} | \varphi_{m\mathbf{k}-\mathbf{q}}^{\sigma} M_{\mathbf{q},I} \rangle \times v_{IJ}(\mathbf{q}) \langle M_{\mathbf{q},J} \varphi_{m\mathbf{k}-\mathbf{q}}^{\sigma} | \varphi_{n'\mathbf{k}}^{\sigma} \rangle, \quad (8)$$

with the usual bra-ket notation $\langle f | g \rangle = \int d^3r f^*(\mathbf{r})g(\mathbf{r})$ and the Coulomb matrix⁴⁴

$$v_{IJ}(\mathbf{q}) = \iint d^3r d^3r' \tilde{M}_{\mathbf{q},I}^*(\mathbf{r}) v(\mathbf{r}, \mathbf{r}') \tilde{M}_{\mathbf{q},J}(\mathbf{r}'). \quad (9)$$

We need to evaluate the latter only once at the beginning of the self-consistency cycle. We note here again that the screening is accounted for in a separate step [cf. Eq. (11)].

As Eq. (8) indicates, the auxiliary basis must be sufficiently complete in the space of wave-function products. We therefore construct this basis directly from products of LAPW basis functions. In the interstitial region, the auxiliary basis functions are plane waves with a new cut-off parameter G'_{\max} and in the MT spheres, the basis consists of numerical functions of the form $M_{LP}^a(r) Y_{LM}(\hat{\mathbf{r}})$ with a cutoff L_{\max} . This so-called mixed product basis (MPB) can be systematically converged to represent the products of LAPW wave functions numerically exactly. In this way, the MPB is on the same level of accuracy as the all-electron LAPW basis for the wave functions. It was shown^{41,54} that G'_{\max} and L_{\max} can be well below their mathematically determined exact limit, i.e., $2G_{\max}$ and $2l_{\max}$, and even below G_{\max} and l_{\max} , which makes the MPB a very efficient basis. Further details about the MPB can be found elsewhere.^{41,44,54}

B. Implementation of the HSE functional

It seems that the implementation of the HSE functional is now straightforward: the bare Coulomb potential in Eq. (9) is replaced by the screened one and it is proceeded as in Ref. 41 for the case of the PBE0 functional. However, in this way we would loose a very favorable property of the bare Coulomb potential, namely, its

multipole expansion, which makes it possible to render

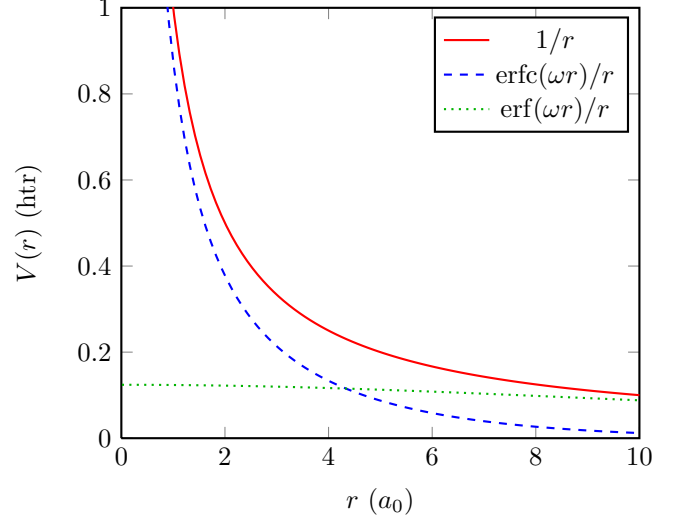


FIG. 1: (Color online) Comparison of the bare (red solid line) and the screened (blue dashed line) Coulomb potentials with the difference between both (green dotted line). The difference does not exhibit a divergence at $r = 0$ and is a smooth function everywhere. Its Fourier transform converges very rapidly.

the Coulomb matrix sparse by a simple unitary transformation of the MPB. The sparsity of $v_{IJ}(\mathbf{q})$ speeds up the matrix-vector multiplications in Eq. (8) considerably. The screened Coulomb potential does not have this simple property. Furthermore, the direct evaluation of $v_{IJ}(\mathbf{q})$ following the techniques of Ref. 44 is not transferable to the screened interaction.

For these reasons, we evaluate Eq. (8) with the bare interaction as before and use a separate step to incorporate the screening. This procedure is motivated by Fig. 1, which shows the bare and screened Coulomb potentials, $v(r)$ and $v^{\text{SR}}(r)$, as well as the difference, $v^{\text{LR}}(r)$, as a function of the distance r , measured in units of Bohr radii a_0 . While the two potentials diverge at $r = 0$, their difference remains finite. It has a very smooth behavior for all distances and should thus be suitable to be described in reciprocal space. In fact, we find that only very few plane waves are needed to represent the difference accurately.

To make use of the quickly converging Fourier expansion of the long-range potential $v^{\text{LR}}(r)$, we rewrite the total xc potential in the form

$$V_{\text{xc}}^{\text{HSE}} = V_{\text{xc}}^{\text{PBE}} - aV_{\text{x}}^{\text{PBE,SR}} + a(V_{\text{x}}^{\text{NL}} - V_{\text{x}}^{\text{NL,LR}}) \quad (10)$$

with the local xc potentials $V_{\text{xc}}^{\text{PBE}}$ and $V_{\text{x}}^{\text{PBE,SR}}$ that derive from $E_{\text{xc}}^{\text{PBE}}$ and $E_{\text{x}}^{\text{PBE,SR}}$, respectively, and the potential terms in the parenthesis sum up to the SR nonlocal potential for HSE as

$$V_{x,nn'}^{\sigma,NL,SR}(\mathbf{k}) = V_{x,nn'}^{\sigma,NL}(\mathbf{k}) + \sum_m^{\text{occ}} \sum_{\mathbf{q}}^{\text{BZ}} \sum_{\mathbf{G}} \langle \varphi_{n\mathbf{k}}^{\sigma} | \varphi_{m\mathbf{k}-\mathbf{q}}^{\sigma} \chi_{\mathbf{q}+\mathbf{G}} \rangle \langle \chi_{\mathbf{q}+\mathbf{G}} | v^{\text{LR}} | \chi_{\mathbf{q}+\mathbf{G}} \rangle \langle \chi_{\mathbf{q}+\mathbf{G}} \varphi_{m\mathbf{k}-\mathbf{q}}^{\sigma} | \varphi_{n'\mathbf{k}}^{\sigma} \rangle, \quad (11)$$

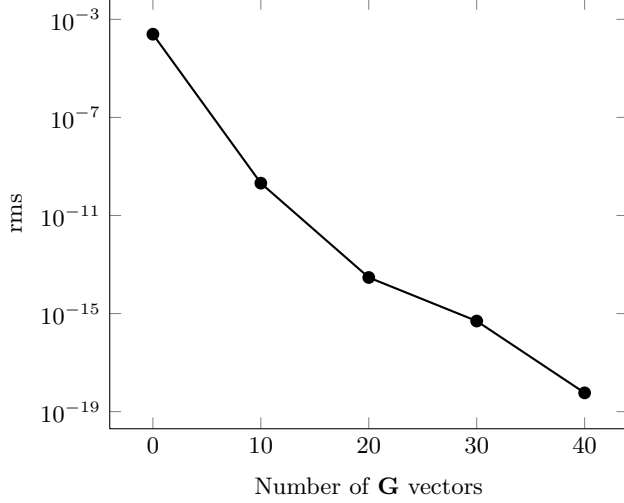


FIG. 2: Root-mean-square (rms) deviation of the eigenvalues of the second term in Eq. (11) from the fully converged result as a function of the number of plane waves in the Fourier transformation for the Γ point of silicon. We have used a supercell containing eight atoms. The 40 Fourier components would translate to ten in a calculation of the primitive unit cell with two atoms.

where $\chi_{\mathbf{q}+\mathbf{G}}(\mathbf{r}) = e^{i(\mathbf{q}+\mathbf{G})\cdot\mathbf{r}} / \sqrt{V}$ is a plane wave normalized by the crystal volume V . We evaluate the Fourier transform of the wave-function products with the help of the MPB

$$\langle \varphi_{n\mathbf{k}}^{\sigma} | \varphi_{m\mathbf{k}-\mathbf{q}}^{\sigma} \chi_{\mathbf{q}+\mathbf{G}} \rangle = \sum_I \langle \varphi_{n\mathbf{k}}^{\sigma} | \varphi_{m\mathbf{k}-\mathbf{q}}^{\sigma} M_{\mathbf{q}I} \rangle \langle \tilde{M}_{\mathbf{q}I} | \chi_{\mathbf{q}+\mathbf{G}} \rangle, \quad (12)$$

where the first integrals on the right-hand side are calculated routinely already for $V_{x,nn'}^{\sigma,NL}$. The Fourier transform of v^{LR} is known analytically

$$\langle \chi_{\mathbf{q}+\mathbf{G}} | v^{\text{LR}} | \chi_{\mathbf{q}+\mathbf{G}'} \rangle = \frac{4\pi}{|\mathbf{q}+\mathbf{G}|^2} e^{-|\mathbf{q}+\mathbf{G}|^2/4\omega^2} \delta_{\mathbf{G}\mathbf{G}'}. \quad (13)$$

We note that any other form of the screened Coulomb interaction could easily be implemented at this stage. Since the matrix elements are diagonal in reciprocal space, the second term of Eq. (11) takes in practical terms negligible time to compute. From the fact that this function approaches zero very quickly with $|\mathbf{q}+\mathbf{G}|$, it is clear that the results are easily converged up to machine precision, even if the Fourier coefficient in Eq. (12) falls off slowly with respect to $|\mathbf{q}+\mathbf{G}|$ because of the rapidly varying all-electron wave functions. Figure 2 shows the root-mean-square deviation of the eigenvalues of the matrix

$V_{x,nn'}^{\sigma,NL,SR}(\mathbf{k}) - V_{x,nn'}^{\sigma,NL}(\mathbf{k})$, as a function of the number of \mathbf{G} vectors used for its construction. The convergence was studied for the case of bulk silicon using a supercell with eight atoms. Machine precision is achieved with as few as 40 plane waves which would translate to ten for a primitive unit cell containing two atoms. This behavior is independent of the \mathbf{q} point.

We note that the Fourier transform in Eq. (13) diverges as $1/|\mathbf{q}+\mathbf{G}|^2$ in the limit $\mathbf{q}+\mathbf{G} \rightarrow \mathbf{0}$. The same divergence is found for the bare Coulomb potential,^{41,44} such that the $1/|\mathbf{q}+\mathbf{G}|^2$ terms cancel in the difference. The remainder is finite and is given by

$$\lim_{\mathbf{q}+\mathbf{G} \rightarrow \mathbf{0}} \frac{4\pi}{|\mathbf{q}+\mathbf{G}|^2} \left(1 - e^{-|\mathbf{q}+\mathbf{G}|^2/4\omega^2} \right) = \frac{\pi}{\omega^2}. \quad (14)$$

We will later see that this nondivergent behavior of the screened interaction gives rise to a favorable \mathbf{k} -point convergence.

IV. VERIFICATION

First, we present calculations for a prototypical set of semiconductors (C, Si, and GaAs) and insulators (MgO, NaCl, and Ar) and compare the results with previous works from the literature.^{35,52} We focus in particular on direct and indirect band transitions. These are calculated as the energy differences of the highest occupied and the lowest unoccupied eigenstates at the corresponding points in the BZ. We have taken the experimental lattice constants from Ref. 55. In Fig. 3, we show the convergence of the band gap for silicon with the size of the \mathbf{k} -point mesh. Within HSE this convergence is almost as fast as in PBE, whereas PBE0 requires larger \mathbf{k} -point meshes. This can be attributed to the nondivergent behavior of the screened interaction at $\mathbf{k} = \mathbf{0}$ (s. Sec. III) and was already observed in Ref. 35. We find that an $8 \times 8 \times 8$ \mathbf{k} -point mesh gives reliable HSE results for the band gap as well as for ground-state properties.

In Table I, we compare our results for the $\Gamma \rightarrow \Gamma$, $\Gamma \rightarrow X$, and $\Gamma \rightarrow L$ transition energies with those obtained by the projector-augmented-wave (PAW) method³⁵ and experimental data. The band transitions are calculated for a set of materials at their experimental lattice constants with the functionals PBE and HSE. Overall, we observe excellent agreement between the calculated values. In comparison to the experimental results, the HSE functional considerably improves on the PBE values. For semiconductors, the HSE transition energies are in very good agreement with experiment, while the larger gaps of insulators are still underestimated.

TABLE I: Kohn-Sham transition energies in eV obtained with the functionals PBE and HSE at experimental lattice constants compared with values from PAW calculations and experiment. An $8 \times 8 \times 8$ \mathbf{k} -point mesh was employed.

		This work		PAW ^a		Expt.
		PBE	HSE	PBE	HSE	
GaAs	$\Gamma \rightarrow \Gamma$	0.54	1.43	0.56	1.45	1.52, ^b 1.63 ^c
	$\Gamma \rightarrow X$	1.47	2.06	1.46	2.02	1.90, ^b 2.01, ^c 2.18 ^c
	$\Gamma \rightarrow L$	1.01	1.78	1.02	1.76	1.74, ^b 1.84, ^c 1.85 ^c
Si	$\Gamma \rightarrow \Gamma$	2.56	3.32	2.57	3.32	3.05, ^d 3.34–3.36, ^e 3.4 ^c
	$\Gamma \rightarrow X$	0.71	1.29	0.71	1.29	1.13, ^e 1.25 ^d
	$\Gamma \rightarrow L$	1.54	2.24	1.54	2.24	2.06, ^f 2.40 ^c
C	$\Gamma \rightarrow \Gamma$	5.60	6.98	5.59	6.97	7.3 ^b
	$\Gamma \rightarrow X$	4.75	5.90	4.76	5.91	—
	$\Gamma \rightarrow L$	8.46	10.02	8.46	10.02	—
MgO	$\Gamma \rightarrow \Gamma$	4.77	6.49	4.75	6.50	7.7 ^g
	$\Gamma \rightarrow X$	9.14	10.86	9.15	10.92	—
	$\Gamma \rightarrow L$	7.93	9.69	7.91	9.64	—
NaCl	$\Gamma \rightarrow \Gamma$	5.20	6.57	5.20	6.55	8.5 ^h
	$\Gamma \rightarrow X$	7.58	9.05	7.60	8.95	—
	$\Gamma \rightarrow L$	7.30	8.66	7.32	8.67	—
Ar	$\Gamma \rightarrow \Gamma$	8.70	10.36	8.68	10.34	14.2 ⁱ

^aReference 35.

^bReference 56

^cReference 57.

^dReference 58.

^eReference 59.

^fReference 60.

^gReference 61.

^hReference 62.

ⁱReference 63.

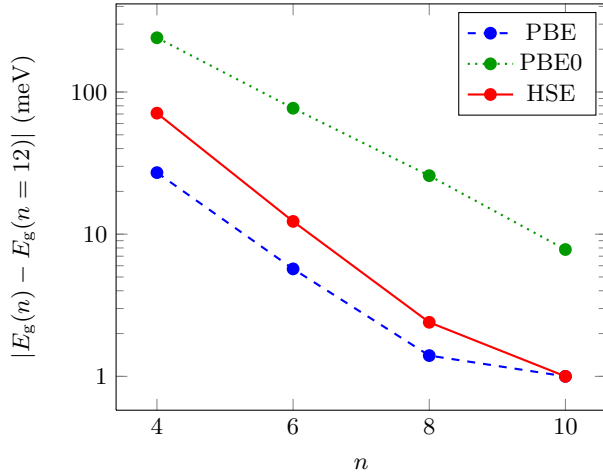


FIG. 3: (Color online) Convergence of the silicon band gap E_g for the functionals PBE (blue, dashed), PBE0 (green, dotted), and HSE (red, solid) with respect to the \mathbf{k} -point mesh ($n \times n \times n$).

We compute the equilibrium lattice constants and bulk moduli by calculating total energies for different lattice constants and fitting the results to the Murnaghan

TABLE II: Optimized lattice constants in Å obtained with the PBE and the HSE functional. An $8 \times 8 \times 8$ \mathbf{k} -point mesh was employed. Results are compared to experimental results and calculations using the HSE functional within a PAW³⁵ and a Gaussian⁵² method.

Functional	This work		PAW ^a	Gaussian ^b	Expt. ^c
	PBE	HSE	HSE	HSE	—
GaAs	5.743	5.660	5.687	5.710	5.648
Si	5.472	5.441	5.435	5.451	5.430
C	3.571	3.549	3.549	3.557	3.567
MgO	4.265	4.217	4.210	4.222	4.207
NaCl	5.703	5.627	5.659	5.645	5.595

^aReference 35.

^bReference 52.

^cExperimental data taken from Ref. 55.

equation of state.⁶⁴ In Table II and Table III, we compare the lattice constants and bulk moduli obtained with our implementation of the HSE functional with results from implementations based on plane-wave (PAW)³⁵ and Gaussian basis sets.⁵² The results of all three methods agree very well. For example the lattice constants calcu-

TABLE III: Bulk moduli in GPa obtained with the PBE and the HSE functional. An $8 \times 8 \times 8$ \mathbf{k} -point mesh was employed. Results are compared to experimental results and calculations using the HSE functional within a PAW method.³⁵

Functional	This work		PAW ^a	Expt. ^b
	PBE	HSE	HSE	—
GaAs	64.5	79.2	70.9	75.6
Si	88.9	98.0	97.7	99.2
C	433	467	467	443
MgO	153	177	169	165
NaCl	21.3	28.8	24.5	26.6

^aReference 35.

^bExperimental data taken from Ref. 55.

TABLE IV: Numerical parameters used for the calculation of GdN.

parameter	value	
\mathbf{k} -point mesh	$8 \times 8 \times 8$	
muffin-tin radii	$R_{\text{MT}}(\text{Gd}) = 2.33 a_0$	$R_{\text{MT}}(\text{N}) = 1.95 a_0$
plane-wave cutoffs	$G_{\text{max}} = 4.9 a_0^{-1}$	$G'_{\text{max}} = 3.6 a_0^{-1}$
angular-momentum	$l_{\text{max}}(\text{Gd}) = 12$	$l_{\text{max}}(\text{N}) = 10$
cutoffs	$L_{\text{max}}(\text{Gd}) = 6$	$L_{\text{max}}(\text{N}) = 4$
local orbitals ^a	Gd: 5s,5p;7s,7p,6d,5f N: 3s,3p,4d,5f	
number of bands	200	

^aReference 65.

lated in the FLAPW and PAW methods differ by less than 3 pm. Except for diamond, the HSE functional yields lattice constants and bulk moduli in much better agreement with experiment than the semilocal PBE functional, which tends to overestimate the former and underestimate the latter.

V. GADOLINIUM NITRIDE

A. Computational setup

GdN crystallizes in the rocksalt structure, with a room-temperature lattice constant of $a_{\text{GdN}} = 4.988 \text{ \AA}$.⁷⁰ The valence band of this material consists of the N $2s$, $2p$ and the Gd $4f$ states. The $4f$ states are only half-occupied. The conduction band is formed by the Gd $5d$ and $6s$ states as well as the $4f$ states in the minority channel.

We determine the numerical cutoff parameters for the calculations in such a way that the difference between the total energies calculated at the experimental lattice constant, a_{GdN} , and at $1.01a_{\text{GdN}}$ changes by less than 1 meV upon increasing the parameters. In Table IV, we list the parameters used for the GdN unit cell (consisting of two atoms). In particular, we converged the \mathbf{k} -point

sampling, the size of the FLAPW basis, the size of the MPB, and the number of local orbitals. The latter are additional basis functions that are used to describe semi-core states⁷² or to eliminate the linearization error.^{73,74}

In the following, we compare our theoretical HSE results for the lattice constant, bulk modulus, band gaps, and magnetic moment with previous calculations and experiment. In order to compare our band structure results obtained at 0 K with the experimental results obtained at room-temperature, where GdN is in the paramagnetic state, we follow the idea that there is no difference between the ferromagnetic and paramagnetic state for the exchange splitting and the large magnetic moments of the $4f$ electrons. In the paramagnetic state we rather assume local magnetic f moments that fluctuate in direction with an overall zero magnetization. Thus, the magnetic polarization of the N states disappears. Dispersive valence and conduction electrons that exhibit a large group velocity feel at any moment in time a small random potential landscape due to the exchange potentials of Gd f moments pointing in random directions. Following Ref. 46 this can be approximated assuming that in the paramagnetic phase each of these s , p , and d valence and conduction states characterized by a \mathbf{k} -point band index are obtained by the averages of the corresponding spin-up and spin-down energies in the ferromagnetic phase.

Furthermore, from the total-energy differences we derive the exchange coupling constants for a Heisenberg spin Hamiltonian and determine the Curie temperature. This gives us a measure for the quality of energy differences that can be expected from the HSE functional between different magnetic states.

B. Structural and electronic properties

We start our investigation of GdN by evaluating its structural and electronic properties and comparing them to some of the available experimental^{10,68–70} and theoretical data, obtained with the hybrid B3LYP functional²³ and within the LSDA+ U approach.^{14,46,68} The comparison is shown in Table V. We note that our parameter-free HSE calculations yield a lattice parameter of 4.967 \AA in very close agreement to the experiment, while B3LYP overestimates the value by $\sim 2\%$ and the lattice constant in the LSDA+ U method depends on the choice of the parameter U . Thermal expansion could account for the remaining difference to the experimental lattice parameter that was determined at the room temperature (whereas the theoretical result corresponds to 0 K). The thermal expansion coefficient of GdN is unknown so far. Assuming linear expansion between 0 K and room temperature (293 K) with the coefficient of isostructural and isovalent EuO ($\approx 13 \times 10^{-6} \text{ K}^{-1}$),⁷⁵ one would extrapolate to 4.969 \AA at 0 K, which is, indeed, very close to our optimized lattice constant.

Next, we turn to the electronic structure. In Fig. 4

TABLE V: Comparison of our HSE results for GdN with those from LSDA+ U and B3LYP calculations and experiment. The theoretical results are given for the optimized lattice constant, unless stated otherwise.

	HSE ^a	HSE	LSDA+ U ^b	LSDA+ U ^c	LSDA+ U ^{a,d}	B3LYP ^e	Expt.
Lattice constant (\AA)	(4.988)	4.967	4.92	5.08	(4.988)	5.05	4.988 ^f
Bulk modulus (GPa)	—	164	—	150	—	159	192 ^g
Magnetic moment (μ_B)	6.99	6.99	—	6.93 ^a	—	7.0	6.88 ^h
Direct gap at X (eV) ($T < T_C$)	0.90	0.85	-0.16 ⁱ	—	0.91	1.18 ⁱ	0.90 ^j
Direct gap at X (eV) ($T > T_C$)	1.17	1.11	0.10 ⁱ	0.98 ^a	1.30	1.77 ⁱ	1.31 ^j
Indirect gap $\Gamma \rightarrow X$ (eV) ($T < T_C$)	0.01	-0.06	-0.45 ⁱ	0.14 ^a	0.43	0.72 ⁱ	—
Indirect gap $\Gamma \rightarrow X$ (eV) ($T > T_C$)	0.90	0.85	-0.13 ⁱ	0.69 ^a	0.98	1.47 ⁱ	—
Position of majority 4 <i>f</i> peak (eV) ^k	-6.00	-6.00	-7.8	-8.1 ^{a,i}	—	-6.3 ⁱ	-7.8 ^l
Position of minority 4 <i>f</i> peak (eV) ^k	6.05	6.05	6.6	5.0 ^{a,i}	4.8 ⁱ	5.5 ⁱ	5.5 – 6.1 ^m

^aAt the experimental lattice constant of 4.988 \AA .

^bReference 14; U optimized for Gd bulk (Ref. 66).

^cReference 46; U chosen to reproduce the experimental direct gap of paramagnetic GdN (Ref. 67).

^dReference 68; U chosen to reproduce the experimental direct gap of paramagnetic GdN.

^eInsulating solution of Ref. 23.

^fAt room temperature; Ref. 69.

^gReference 70.

^hReference 10

ⁱExtracted from the band structure.

^jReference 68.

^kRelative to the top of the valence band.

^lReference 11.

^mReference 71 measured for GdX (X = P, As, Sb, and Bi).

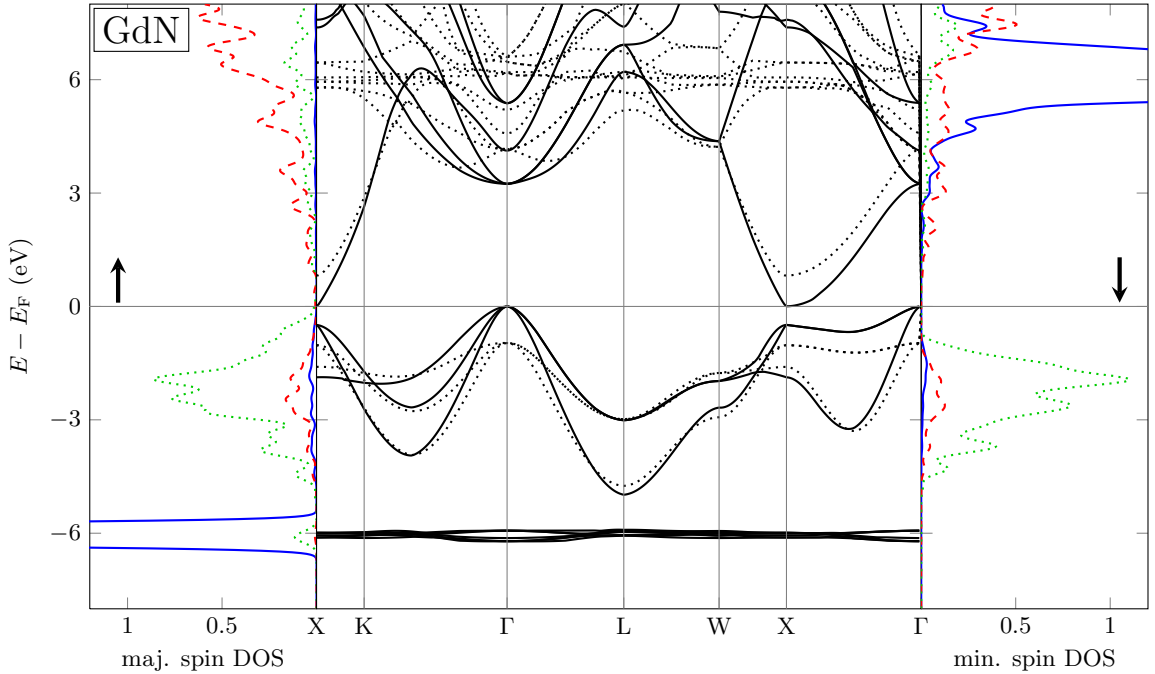


FIG. 4: (Color online) Band structure and density of states (DOS; in states per eV) of GdN at the experimental lattice constant. The majority and minority bands are plotted as solid and dotted lines, respectively. The orbital-resolved DOS is shown on the left for majority and on the right for minority states. The solid blue line shows the Gd 4*f* states, the red dashed line the Gd 5*d* states, and the green dotted line the N 2*p* states.

we show the spin-resolved band structure and the spin- and orbitally resolved density of states calculated at the experimental lattice constant (4.988 Å). At about -6 eV and $+6$ eV we find the localized majority and minority Gd $4f$ state, respectively. In the vicinity of the Fermi energy, GdN exhibits a truly interesting electronic structure. Of particular interest are a direct and an indirect band gap, discussed extensively in the literature. The direct band gap accessible by optical measurements is located at the X point and amounts to 0.9 eV for the majority spin channel and 1.5 eV for the minority spin channel. The valence and the conduction states are separated by an indirect band gap ($\Gamma \rightarrow X$): In the minority-spin states, this is a robust band gap of 1.5 eV, while in the majority-spin states this gap is tiny, only 0.01 eV. Thus, we observe that GdN is in a narrow-gap semiconducting ground state with an almost vanishing indirect band gap ($\Gamma \rightarrow X$) in the majority-spin direction, between the N $2p$ states in the valence and the Gd $5d$ states in the conduction band. This explains the different experimental reports disclosing GdN as a low carrier semimetal or an insulator depending on small changes of the experimental circumstances.

Upon decreasing the lattice constant isotropically by just 0.02 Å to the theoretically optimized value of 4.967 Å, we observe a transition to a half-metallic state or, more precisely, to a semimetallic state just for the majority states: a small portion of the N $2p$ states at the Γ point remains unoccupied, while the Gd $5d$ band becomes partially occupied at the X point. If we define the “band gap” as the difference of these states, we formally get its value to be negative (see the band-transition energies in Table V). The described transition from a half-metallic to semiconducting state under isotropic strain was also observed by Duan *et al.*,¹⁴ however at a much larger lattice constant of 5.63 Å. Our results suggest that, since the semiconductor to half-metal transition occurs so close to the equilibrium lattice parameter, the growth conditions, which influence the material properties such as the concentration of possible N vacancies or strain in the system, or the lattice expansion upon temperature changes play a decisive role in the transport properties of GdN.

Interesting physics can be expected also upon doping. If we n-dope into the conduction band or p-dope into the valence band, e.g. by use of Eu, at a concentration where electrons or holes populate only majority states, we can obtain significant charge currents with 100% spin polarization. In the paramagnetic phase, minority and majority states converge to spin-degenerate valence and conduction states, and any spin polarization of the charge current disappears. At the same time, the band gap opens in the paramagnetic state, partly because of the thermal expansion and partly because of the averaged-out exchange potential felt by the electrons. This, and a possible coupling of the conduction electrons or holes to the fluctuating $4f$ moments⁷⁶ may change the conductivity by orders of magnitude when passing through the Curie temperature (T_C).

In Table V, we list the band-transition energies calculated with our method at the experimental and at the optimized lattice constant for the ferromagnetic ($T < T_C$) and the paramagnetic ($T > T_C$) state. We find invariably larger band gaps for the paramagnetic state with no transition to a metallic state nearby. Our calculated band-transition energies compare well with the experimental data where available. The small indirect majority spin gap between Γ and X of 0.01 eV compares well with estimates of 0.05 eV from Chantis *et al.*⁷⁷ obtained using the quasiparticle self-consistent *GW* method (QSGW) combined with their empirical rule to estimate band gaps in semiconductors. The transition energies obtained within the LSDA+*U* method depend strongly on the choice of the parameter *U*. At the experimental lattice constant, we find similar transition energies as in the works of Larson *et al.*⁴⁶ and Trodahl *et al.*,⁶⁸ where in the latter the parameter *U* applied to the $4f$ electrons was chosen to agree with the differences of the binding energies of the occupied and unoccupied $4f$ level as measured with the X-ray photoemission and inverse photoemission, respectively, in the Gd pnictides and the *U* applied to Gd d states was chosen to reproduce the direct experimental band gap in the paramagnetic phase. In this way, the redshift of the direct band gap of 0.41 eV going from the paramagnetic state to the ferromagnetic state is perfectly reproduced, while our parameter-free calculation gives 0.27 eV. The crossing of the conduction and the valence band at the X point was obtained with smaller values of *U*,¹⁴ whereas we find a direct band gap at X even below the Curie temperature T_C . The calculation with B3LYP²³ yields three different solutions, where only the insulating one is similar to our result. The band gaps are significantly larger which may be attributed to the larger optimized lattice constant.

The binding energy of the Gd $4f$ majority band is also improved in the HSE scheme: the partial compensation of the self-interaction error leads to a pronounced shift of the localized $4f$ states to larger binding energies. Calculation with the PBE functional yields a much too shallow f majority band, located at 3.1 eV below the Fermi energy; in HSE this band appears at a binding energy of 6.0 eV, much closer to its experimentally measured position at 7.8 eV.¹¹ Furthermore, we note a very good agreement with the insulating B3LYP result, where the position of the $4f$ peak is found at 6.3 eV.²³ However, the agreement with experiment is not perfect. For the f systems a stronger mixing of nonlocal exchange would probably give a better result. As compared to PBE results, the unoccupied $4f$ minority states shift towards higher energies (6.05 eV), which is consistent with previous LSDA+*U* and B3LYP calculations.^{14,23,46} The position of the unoccupied $4f$ states agrees well with typical experimental results for the gadolinium pnictides between 5.5 eV and 6.1 eV obtained with inverse photoemission spectroscopy.⁷¹

C. Magnetic order and critical temperature

The ground state of unconstrained bulk GdN is ferromagnetic (FM), with a Curie temperature of 58 K⁷⁰ and a magnetic moment of $6.88 \mu_B$ per Gd atom¹⁰ determined from the saturation magnetization at 1.2 K. The total calculated magnetic moment is $7 \mu_B$ per formula unit of which $6.99 \mu_B$ comes from the Gd muffin-tin sphere. Our results are in good agreement with these observations (see the comparison of the theoretical and experimental values of the magnetic moment in Table V). We confirm the magnetic order and determine the critical temperature by mapping the total energies obtained from our HSE calculations for several magnetic structures onto the classical Heisenberg Hamiltonian

$$\mathcal{H} = -\frac{1}{2} \sum_i \mathbf{S}_i \left(J_1 \sum_{j=\text{nn}} \mathbf{S}_j + J_2 \sum_{j=\text{nnn}} \mathbf{S}_j \right) \quad (15)$$

including the nearest neighbors (nn), and the next nearest neighbors (nnn) interaction where J_1 and J_2 are the respective coupling constants with normalized spin vectors \mathbf{S}_i and \mathbf{S}_j . Positive and negative values of J favor parallel and antiparallel spin alignment, respectively. The coupling constants are extracted from the differences of the total energies of the FM, and two types of antiferromagnetic (AFM) configurations characterized by planes of ferromagnetically ordered moments that are antiferromagnetically stacked along the crystallographic [001] or [111] directions (AFM-I and AFM-II, respectively).¹⁴ For the calculation of the AFM-I (AFM-II) phase we use a tetragonal $1 \times 1 \times 2$ (trigonal $\sqrt[3]{2} \times \sqrt[3]{2} \times \sqrt[3]{2}$) unit cell containing two Gd atoms and calculate the FM state in the same unit cells, in order to guarantee reliable total energy differences. All the calculations are performed at the experimental lattice constant.

From the expressions

$$\Delta E_I = E_{\text{AFM},I} - E_{\text{FM},I} = 8J_1 \quad (16)$$

$$\Delta E_{II} = E_{\text{AFM},II} - E_{\text{FM},II} = 6J_1 + 6J_2, \quad (17)$$

the Heisenberg coupling constants J_1 and J_2 are easily obtained. We list them in Table VI, along with their values calculated in previous studies using an LSDA+ U method within an FLAPW¹⁴ and an LMT0 basis set.¹² Both coupling constants are positive, confirming the ferromagnetic nature of the ground state.

We use two approaches to estimate the Curie temperature. In the mean-field approximation (MFA)

$$T_C^{\text{MFA}} = \frac{1}{3k_B} (12J_1 + 6J_2), \quad (18)$$

we obtain a $T_C^{\text{MFA}} = 55$ K, very close to the experimental value of 58 K.⁷⁰ It is known, however, that the mean-field theory overestimates the Curie temperature. For comparison, we have also calculated the critical temperature by employing the random phase approximation (RPA)

TABLE VI: Differences of total energies for different magnetic configurations [Eqs. (16) and (17)], the Heisenberg coupling constants, and the corresponding Curie temperatures within the mean-field approximation [Eq. (18)] and random phase approximation [Eq. (19)]. Energies and coupling constants are given in meV and the Curie temperatures in K.

	ΔE_I	ΔE_{II}	J_1	J_2	T_C^{MFA}	T_C^{RPA}
This work	8.8	7.6	1.09	0.17	55	42
Duan <i>et al.</i> ^a	6.7	4.2	0.84	-0.14	36	26
Mitra <i>et al.</i> ^b	3.4	0.4	0.42	-0.36	11	5

^aReference 14.

^bReference 12.

as described in Refs. 78 and 79, which is known to give results close to Monte Carlo solution:

$$T_C^{\text{RPA}} = \frac{1}{3k_B} \left[\int_{\text{BZ}} d^3q \frac{1}{J(\mathbf{0}) - J(\mathbf{q})} \right]^{-1}, \quad (19)$$

where we evaluate the integral on a discrete mesh of \mathbf{q} points within the Brillouin zone. $J(\mathbf{q})$ is the Fourier transform of the exchange coupling constants defined as

$$J(\mathbf{q}) = \sum_{\text{nn}} J_1 e^{i\mathbf{q} \cdot \mathbf{R}_{\text{nn}}} + \sum_{\text{nnn}} J_2 e^{i\mathbf{q} \cdot \mathbf{R}_{\text{nnn}}}, \quad (20)$$

where \mathbf{R}_{nn} and \mathbf{R}_{nnn} are the positions of the nearest and the next nearest neighbors, respectively. The resulting $T_C^{\text{RPA}} = 42$ K is roughly 30% smaller than the mean-field estimate. We consider these results as a sophisticated theoretical estimation of the Curie temperature that goes along with a few uncertainties, some of which are difficult to assess, such as the quality of HSE being an approximation to the true but unknown exchange and correlation functional and to a much lesser extent the adiabatic approximation inherent in applying the Heisenberg model. Easier to assess are technically induced error estimates: (i) ΔE in Eqs. (16) and (17) are converged to about 1 meV, which translates to an uncertainty of 3 K. (ii) Based on Monte Carlo calculations with two (as given in Table VI) and three nearest neighbors employing coupling constants published by Duan *et al.*,¹⁴ which in both cases lead to the same Curie temperature of 28 K, we estimate that the neglect of exchange interactions beyond next nearest neighbors leads to a maximum uncertainty of 1 K. (iii) Employing our coupling constants (as given in Table VI), we find that the RPA result of 42 K approximates the numerically precise determination of the Curie temperature within the Heisenberg model obtained by Monte Carlo, 45 K, by 3 K.

With these error estimates in mind, we compare our values to results of experimental studies, e.g. $T_C = 68, 69, 58$ or 37 K as reported by Granville *et al.*,¹⁷ Khazen *et al.*,⁸⁰ Leuenberger *et al.*,¹¹ and Yoshitomi *et al.*,⁸¹ which vary in value also depending on film thickness, strain, grain size, stoichiometry, and N vacancies.^{82,83}

We conclude that our results are in very good agreement with the experimental situation. Comparing our results to other theoretical values exhibited in Table VI we note that our coupling constants J_1 and J_2 obtained with HSE are significantly higher which gives rise to a higher Curie temperature, in agreement with experiment. We observe that the increase of the coupling constants goes along with an increase of the Gd $4f$ moment in the muffin-tin sphere by $90 \text{ m}\mu_B$ from $6.78 \mu_B$ to $6.87 \mu_B$, a decrease of the Gd $5d$ moment by $20 \text{ m}\mu_B$ from $90 \text{ m}\mu_B$ to $70 \text{ m}\mu_B$, and an increase of the N $2p$ moment, which is aligned antiparallel to the Gd $4f$ moment, by $20 \text{ m}\mu_B$, from $-100 \text{ m}\mu_B$ to $-120 \text{ m}\mu_B$, when HSE is compared to the PBE functional. The precise understanding of the relationship between the change of the moments and the coupling constants requires additional analysis that goes beyond the scope of the paper.

VI. CONCLUSION

In this work, we have presented an implementation of the HSE hybrid functional, which contains a nonlocal screened exchange potential, within the FLAPW method as implemented in the *Fleur* code.³⁶ The calculation of the nonlocal exchange potential is realized by projecting the wave-function products onto the mixed product basis, reducing the six-dimensional integrations over the non-local interaction potential to vector-matrix-vector products, where the matrix must be calculated only once at the beginning of the self-consistent-field cycle.

We employ a sparse-matrix technique⁴¹ to evaluate the vector-matrix-vector products and incorporate the screening, i.e., the long-range part of the potential, in a separate step, where we exploit its fast converging Fourier series. This procedure allows constructing the nonlocal HSE potential from PBE0 up to machine precision at a negligible computational cost. We note that this approach is not restricted to the error function used in the HSE functional. In fact, our approach is quite general, it can be easily applied to arbitrarily screened interaction potentials.

The results for lattice constants and band-transition

energies obtained within our method show excellent agreement with previous results obtained with the PAW³⁵ and Gaussian-based⁵² methods. We have confirmed the finding of Paier *et al.*³⁵ that the \mathbf{k} -point convergence within HSE is comparable to the conventional local PBE functional, whereas in PBE0 much larger \mathbf{k} -point meshes are necessary.

In addition, we have calculated the properties of the rare-earth compound GdN. There is an ongoing discussion whether the ground state is insulating or metallic. In fact, within the HSE functional the ground state is very close to a phase transition: we observe a tiny indirect band gap at the experimental lattice constant at room temperature, which vanishes at the theoretically optimized 0 K lattice constant – the compound becomes half-metallic. The experimentally known band transitions are in good agreement with our theoretical results. Furthermore, we have calculated the coupling constants for the Heisenberg spin Hamiltonian from total-energy differences of ferromagnetic and antiferromagnetic configurations. The resulting Curie temperature of 42 K evaluated in the random-phase approximation is in good agreement with the experimental value of 58 K and gives confidence in the energetics obtained by HSE for different magnetic phases. From this we conclude that the HSE functional has the potential to describe the properties of rare-earth chalcogenides without the need for employing a Hubbard U parameter. We encourage the community to make use of the potential of the HSE functional to explore the more subtle properties of the rare-earth chalcogenides such as the physics due to strain, dopands, or heterostructures.

Acknowledgments

We would like to thank Walter Lambrecht for fruitful discussions on GdN. We gratefully acknowledge the funding by the Young Investigators Group Programme of the Helmholtz Association (“Computational Nanofronics Laboratory,” Contract VH-NG-409) and by the Deutsche Forschungsgemeinschaft through the Priority Program 1145.

* Electronic address: m.schlipf@fz-juelich.de

¹ P. Hohenberg and W. Kohn, Phys. Rev. **136**, B864 (1964).

² W. Kohn and L. J. Sham, Phys. Rev. **140**, A1133 (1965).

³ U. von Barth and L. Hedin, J. Phys. C: Solid State Phys. **5**, 1629 (1972).

⁴ O. Gunnarsson and B. I. Lundqvist, Phys. Rev. B **13**, 4274 (1976).

⁵ D. M. Ceperley and B. J. Alder, Phys. Rev. Lett. **45**, 566 (1980).

⁶ J. P. Perdew and Y. Wang, Phys. Rev. B **33**, 8800 (1986).

⁷ J. P. Perdew, K. Burke, and M. Ernzerhof, Phys. Rev. Lett. **77**, 3865 (1996).

⁸ E. Fermi and E. Amaldi, Accad. Ital. Rome **6**, 119 (1934).

⁹ J. P. Perdew and A. Zunger, Phys. Rev. B **23**, 5048 (1981).

¹⁰ D. X. Li, Y. Haga, H. Shida, and T. Suzuki, Physica B: Condensed Matter **199-200**, 631 (1994).

¹¹ F. Leuenberger, A. Parge, W. Felsch, K. Fauth, and M. Hessler, Phys. Rev. B **72**, 014427 (2005).

¹² C. Mitra and W. R. L. Lambrecht, Phys. Rev. B **78**, 134421 (2008).

¹³ A. Sharma and W. Nolting, Phys. Rev. B **81**, 125303 (2010).

¹⁴ C.-G. Duan, R. F. Sabiryanov, J. Liu, W. N. Mei, P. A. Dowben, and J. R. Hardy, Phys. Rev. Lett. **94**, 237201 (2005).

- (2005); C.-G. Duan, R. F. Sabiryanov, W. N. Mei, P. A. Dowben, S. S. Jaswal, and E. Y. Tsybal, Appl. Phys. Lett. **88**, 182505 (2006); J. Phys.: Condens. Matter. **19**, 315220 (2007).
- ¹⁵ P. Wachter and E. Kaldis, Solid State Commun. **34**, 241 (1980).
 - ¹⁶ J. Q. Xiao and C. L. Chien, Phys. Rev. Lett. **76**, 1727 (1996).
 - ¹⁷ S. Granville, B. J. Ruck, F. Budde, A. Koo, D. J. Pringle, F. Kuchler, A. R. H. Preston, D. H. Housden, N. Lund, A. Bittar, G. V. M. Williams, and H. J. Trodahl, Phys. Rev. B **73**, 235335 (2006).
 - ¹⁸ B. M. Ludbrook, I. L. Farrell, M. Kuebel, B. J. Ruck, A. R. H. Preston, H. J. Trodahl, L. Ranno, R. J. Reeves, and S. M. Durbin, J. Appl. Phys. **106**, 063910 (2009).
 - ¹⁹ M. Scarpulla, C. Gallinat, S. Mack, J. Speck, and A. Gosard, J. Cryst. Growth **311**, 1239 (2009).
 - ²⁰ W. R. L. Lambrecht, Phys. Rev. B **62**, 13538 (2000).
 - ²¹ D. B. Ghosh, M. De, and S. K. De, Phys. Rev. B **72**, 045140 (2005).
 - ²² C. M. Aerts, P. Strange, M. Horne, W. M. Temmerman, Z. Szotek, and A. Svane, Phys. Rev. B **69**, 045115 (2004).
 - ²³ K. Doll, J. Phys.: Condens. Matter **20**, 075214 (2008).
 - ²⁴ V. I. Anisimov, F. Aryasetiawan, and A. I. Lichtenstein, J. Phys.: Condens. Matter **9**, 767 (1997).
 - ²⁵ P. H. Dederichs, S. Blügel, R. Zeller, and H. Akai, Phys. Rev. Lett. **53**, 2512 (1984).
 - ²⁶ M. Cococcioni and S. de Gironcoli, Phys. Rev. B **71**, 035105 (2005).
 - ²⁷ E. Şaşıoğlu, C. Friedrich, and S. Blügel, Phys. Rev. B **83**, 121101 (2011).
 - ²⁸ A. Rohrbach, J. Hafner, and G. Kresse, J. Phys.: Condens. Matter **15**, 979 (2003).
 - ²⁹ J. Muscat, A. Wander, and N. Harrison, Chemical Physics Letters **342**, 397 (2001).
 - ³⁰ E. N. Brothers, A. F. Izmaylov, J. O. Normand, V. Barone, and G. E. Scuseria, J. Chem. Phys. **129**, 011102 (2008).
 - ³¹ A. D. Becke, J. Chem. Phys. **98**, 1372 (1993); *ibid.* **98**, 5648 (1993).
 - ³² J. P. Perdew, M. Ernzerhof, and K. Burke, J. Chem. Phys. **105**, 9982 (1996).
 - ³³ J. Heyd, G. E. Scuseria, and M. Ernzerhof, J. Chem. Phys. **118**, 8207 (2003).
 - ³⁴ J. Paier, R. Hirschl, M. Marsman, and G. Kresse, J. Chem. Phys. **122**, 1 (2005).
 - ³⁵ J. Paier, M. Marsman, K. Hummer, G. Kresse, I. C. Gerber, and J. G. Ángyán, J. Chem. Phys. **124**, 154709 (2006); *ibid.* **124**, 249901 (2006).
 - ³⁶ <http://www.flapw.de>.
 - ³⁷ E. Wimmer, H. Krakauer, M. Weinert, and A. J. Freeman, Phys. Rev. B **24**, 864 (1981).
 - ³⁸ M. Weinert, E. Wimmer, and A. J. Freeman, Phys. Rev. B **26**, 4571 (1982).
 - ³⁹ H. J. F. Jansen and A. J. Freeman, Phys. Rev. B **30**, 561 (1984).
 - ⁴⁰ F. Tran, P. Blaha, K. Schwarz, and P. Novák, Phys. Rev. B **74**, 155108 (2006).
 - ⁴¹ M. Betzinger, C. Friedrich, and S. Blügel, Phys. Rev. B **81**, 195117 (2010).
 - ⁴² F. Tran and P. Blaha, Phys. Rev. B **83**, 235118 (2011).
 - ⁴³ M. Weinert, J. Math. Phys. **22**, 2433 (1981).
 - ⁴⁴ C. Friedrich, A. Schindlmayr, and S. Blügel, Comput. Phys. Commun. **180**, 347 (2009).
 - ⁴⁵ P. Larson and W. R. L. Lambrecht, Phys. Rev. B **74**, 085108 (2006).
 - ⁴⁶ P. Larson, W. R. L. Lambrecht, A. Chantis, and M. van Schilfgaarde, Phys. Rev. B **75**, 045114 (2007).
 - ⁴⁷ J. Harris and R. O. Jones, Journal of Physics F: Metal Physics **4**, 1170 (1974).
 - ⁴⁸ D. C. Langreth and J. P. Perdew, Phys. Rev. B **15**, 2884 (1977).
 - ⁴⁹ A. D. Becke, J. Chem. Phys. **104**, 1040 (1996).
 - ⁵⁰ B. G. Janesko, T. M. Henderson, and G. E. Scuseria, Phys. Chem. Chem. Phys. **11**, 443 (2009).
 - ⁵¹ J. Heyd and G. E. Scuseria, J. Chem. Phys. **120**, 7274 (2004).
 - ⁵² A. V. Krukau, O. A. Vydrov, A. F. Izmaylov, and G. E. Scuseria, J. Chem. Phys. **125**, 224106 (2006).
 - ⁵³ A. Seidl, A. Görling, P. Vogl, J. A. Majewski, and M. Levy, Phys. Rev. B **53**, 3764 (1996).
 - ⁵⁴ C. Friedrich, S. Blügel, and A. Schindlmayr, Phys. Rev. B **81**, 125102 (2010).
 - ⁵⁵ J. Heyd and G. E. Scuseria, J. Chem. Phys. **121**, 1187 (2004).
 - ⁵⁶ *Numerical Data and Functional Relationships in Science and Technology*, Vol. 17 & 22 of *Landolt-Börnstein - Group III Condensed Matter*, edited by K.-H. Hellwege, O. Madelung, M. Schulz, and H. Weiss (Springer-Verlag, New York, 1982).
 - ⁵⁷ T. Chiang and F. J. Himpsel, in *Electronic Structure of Solids: Photoemission Spectra and Related Data*, Vol. 23a of *Landolt-Börnstein - Group III: Condensed Matter*, edited by A. Goldmann and E.-E. Koch (Springer-Verlag, Berlin, 1989).
 - ⁵⁸ J. E. Ortega and F. J. Himpsel, Phys. Rev. B **47**, 2130 (1993).
 - ⁵⁹ M. Welkowsky and R. Braunstein, Phys. Rev. B **5**, 497 (1972).
 - ⁶⁰ R. Hulthén and N. G. Nilsson, Solid State Commun. **18**, 1341 (1976).
 - ⁶¹ S. Adachi, *Optical Properties of Crystalline and Amorphous Semiconductors: Numerical Data and Graphical Information* (Kluwer Academic, Dordrecht, 1999).
 - ⁶² R. T. Poole, J. Liesegang, R. C. G. Leckey, and J. G. Jenkin, Phys. Rev. B **11**, 5190 (1975).
 - ⁶³ R. J. Magyar, A. Fleszar, and E. K. U. Gross, Phys. Rev. B **69**, 045111 (2004).
 - ⁶⁴ F. Murnaghan, Proc. Nat. Acad. Sci. USA **30**, 244 (1944).
 - ⁶⁵ M. Betzinger, C. Friedrich, S. Blügel, and A. Görling, Phys. Rev. B **83**, 045105 (2011).
 - ⁶⁶ B. N. Harmon, V. P. Antropov, A. I. Liechtenstein, I. V. Solovyev, and V. I. Anisimov, J. Phys. Chem. Solids **56**, 1521 (1995); proceedings of the 1994 Conference on Magneto-optic Materials.
 - ⁶⁷ F. Hullinger, in *Handbook on the Physics and Chemistry of Rare Earths*, edited by K. A. J. Gschneider and E. L. (North-Holland Physics Publishing, New York, 1979), Vol. 4, pp. 153–236.
 - ⁶⁸ H. J. Trodahl, A. R. H. Preston, J. Zhong, B. J. Ruck, N. M. Strickland, C. Mitra, and W. R. L. Lambrecht, Phys. Rev. B **76**, 085211 (2007).
 - ⁶⁹ R. C. Brown and N. J. Clark, J. Inorg. Nucl. Chem. **36**, 2507 (1974).
 - ⁷⁰ U. Rössler and D. Strauch, *Group IV Elements, IV-IV and III-V Compounds. Part a - Lattice Properties*, Vol. 41A1a of *Landolt-Börnstein - Group III Condensed Matter* (Springer-Verlag, Berlin, 2001).
 - ⁷¹ H. Yamada, T. Fukawa, T. Muro, Y. Tanaka, S. Imada, S.

- Suga, D.-X. Li, and T. Suzuki, J. Phys. Soc. Jpn. **65**, 1000 (1996).
- ⁷² D. Singh, Phys. Rev. B **43**, 6388 (1991).
- ⁷³ E. E. Krasovskii, Phys. Rev. B **56**, 12866 (1997).
- ⁷⁴ C. Friedrich, A. Schindlmayr, S. Blügel, and T. Kotani, Phys. Rev. B **74**, 045104 (2006).
- ⁷⁵ F. Lévy, Phys. Kondens. Mater. **10**, 71 (1969).
- ⁷⁶ M. Arnold and J. Kroha, Phys. Rev. Lett. **100**, 046404 (2008).
- ⁷⁷ A. N. Chantis, M. van Schilfgaarde, and T. Kotani, Phys. Rev. B **76**, 165126 (2007).
- ⁷⁸ N. N. Bogoliubov and S. V. Tyablikov, Dokl. Akad. Nauk SSSR **126**, 53 (1959).
- ⁷⁹ U. Nowak, in *Magnetism goes Nano*, Vol. 26 of *Matter and Materials*, edited by S. Blügel, T. Brückel, and C. M. Schneider (Forschungszentrum Jülich, Jülich, 2005), p. A3.1.
- ⁸⁰ K. Khazen, H. J. von Bardeleben, J. L. Cantin, A. Bittar, S. Granville, H. J. Trodahl, and B. J. Ruck, Phys. Rev. B **74**, 245330 (2006).
- ⁸¹ H. Yoshitomi, S. Kitayama, T. Kita, O. Wada, M. Fujisawa, H. Ohta, and T. Sakurai, Phys. Rev. B **83**, 155202 (2011).
- ⁸² K. Senapati, T. Fix, M. E. Vickers, M. G. Blamire, and Z. H. Barber, Phys. Rev. B **83**, 014403 (2011).
- ⁸³ A. Punya, T. Cheiwchanchamnangij, A. Thiess, and W. R. L. Lambrecht, MRS Proceedings **1290**, mrsf10-1290-i04-04 (2011).